



HAL
open science

Spontaneous generation of ductile shear zones by thermal softening: Localization criterion, 1D to 3D modelling and application to the lithosphere

Daniel Kiss, Yuri Podladchikov, Thibault Duretz, Stefan M Schmalholz

► To cite this version:

Daniel Kiss, Yuri Podladchikov, Thibault Duretz, Stefan M Schmalholz. Spontaneous generation of ductile shear zones by thermal softening: Localization criterion, 1D to 3D modelling and application to the lithosphere. *Earth and Planetary Science Letters*, 2019, 519, pp.284-296. 10.1016/j.epsl.2019.05.026 . insu-02147766

HAL Id: insu-02147766

<https://insu.hal.science/insu-02147766>

Submitted on 5 Nov 2019

HAL is a multi-disciplinary open access archive for the deposit and dissemination of scientific research documents, whether they are published or not. The documents may come from teaching and research institutions in France or abroad, or from public or private research centers.

L'archive ouverte pluridisciplinaire **HAL**, est destinée au dépôt et à la diffusion de documents scientifiques de niveau recherche, publiés ou non, émanant des établissements d'enseignement et de recherche français ou étrangers, des laboratoires publics ou privés.

Spontaneous generation of ductile shear zones by thermal softening: localization criterion, 1D to 3D modelling and application to the lithosphere

Dániel Kiss^{a,*}, Yuri Podladchikov^a, Thibault Duretz^{a,b}, Stefan M. Schmalholz^a

^a*Institute of Earth Sciences, University of Lausanne, 1015 Lausanne, Switzerland*

^b*Univ Rennes, CNRS, Géosciences Rennes - UMR 6118, F-35000 Rennes, France*

Abstract

The generation of ductile shear zones is essential for the formation of tectonic plate boundaries, such as subduction or strike-slip zones. However, the primary mechanism of ductile strain localization is still contentious. We study here the spontaneous generation of ductile shear zones by thermal softening using thermo-mechanical numerical simulations for linear and power-law viscous flow in one-dimension (1D), 2D and 3D. All models are velocity-driven. The 1D model exhibits bulk simple shear whereas the 2D and 3D models exhibit bulk pure shear. The initial conditions include a small temperature perturbation in otherwise homogeneous material. We use a series of 1D simulations to determine a new analytical formula which predicts the temperature evolution inside the shear zone. This temperature prediction requires knowledge of only the boundary velocity, flow law and thermal parameters, but no *a priori* information about the shear zone itself, such as thickness, stress and strain rate. The prediction is valid for 1D, 2D and 3D shear zones in bulk pure and simple shear. The results show that shear heating dominates over conductive cooling if the relative temperature increase is > 50 °C.

*corresponding author (daniel.kiss@unil.ch)

The temperature variation induced by the shear zone is nearly one order of magnitude wider than the corresponding finite strain variation so that no significant temperature variation occurs between shear zone and wall rock. Applying typical flow laws for lithospheric rocks shows that shear zone generation by thermal softening occurs for typical plate tectonic velocities of few cm.yr^{-1} or strain rates between 10^{-16} and 10^{-14} s^{-1} . Shear stresses larger than 200 MPa can already cause strain localization. The results indicate that thermal softening is a feasible mechanism for spontaneous ductile shear zone generation in the lithosphere and may be one of the primary mechanisms of lithospheric strain localization.

Keywords: Ductile shear zone, thermal softening, strain localization, shear heating, localization criterion, subduction initiation

1. Introduction

2 The spontaneous generation of shear zones in ductile rocks is fundamental
3 for the formation of tectonic plate boundaries, such as subduction and strike slip
4 zones, or the generation of tectonic nappes during orogenic wedge formation.
5 We refer here to spontaneous generation of a shear zone when the fundamen-
6 tal shear zone parameters, such as thickness, shear stress and strain rate, are not
7 *a priori* prescribed by the natural or model configuration. We refer to ductile
8 deformation when the deformation behaviour is described mathematically by a
9 relation between stress and strain rate, such as by flow laws for diffusion, dislo-
10 cation or Peierls creep (i.e. low temperature plasticity). The conversion of dis-
11 sipative work into heat, the related local temperature increase and the associated
12 decrease of temperature dependent rock viscosities has frequently been suggested
13 as a cause of spontaneous strain localization and shear zone formation in the litho-

14 sphere (Yuen et al., 1978; Regenauer-Lieb and Yuen, 1998; Leloup et al., 1999;
15 Kaus and Podladchikov, 2006; Takeuchi and Fialko, 2012; Thielmann and Kaus,
16 2012; Duretz et al., 2015; Jaquet et al., 2015; Moore and Parsons, 2015). We
17 refer here to this thermally controlled strain localization mechanism as thermal
18 softening. Despite its fundamental thermo-mechanical feasibility (Hersey, 1936;
19 Brinkman, 1951; Grunfest, 1963), shear heating and thermal softening is still
20 contentious as important softening mechanism causing strain localization in duc-
21 tile rock (Regenauer-Lieb et al., 2001; Platt and Behr, 2011; Bercovici and Ricard,
22 2012; Ghazian and Buiter, 2013; Gueydan et al., 2014; Platt, 2015). This is, for
23 example, different from physics-based models of friction in rock where essen-
24 tially all potential processes causing significant friction weakening are considered
25 to be related to shear heating, such as "flash heating", thermal pressurization or
26 temperature controlled chemical/phase changes, including melting and formation
27 of pseudotachylites (Sibson, 1975; Fialko and Khazan, 2005; Brown and Fialko,
28 2012; Aharonov and Scholz, 2018). For ductile strain localization, proposed al-
29 ternative mechanisms not related to shear heating are, for example, grain size re-
30 duction (Bercovici and Ricard, 2012; Platt, 2015), reaction-weakening caused by
31 infiltration of fluids along precursor brittle faults (White and Knipe, 1978; Manck-
32 telow and Pennacchioni, 2005) or fabric development in rock with significant me-
33 chanical heterogeneities (Montési, 2013). Out of the different mechanisms pro-
34 posed for ductile strain localization, shear heating and thermal softening (1) must
35 occur in nature since dissipative deformation generates heat and rock viscosity
36 is temperature dependent and (2) requires the least assumptions since no knowl-
37 edge concerning grain size reduction and growth, fluid flow, reaction kinetics or
38 mechanical heterogeneities required for fabric evolution is needed. Hence, ther-

39 mal softening as mechanism itself is actually not contentious, but whether thermal
40 softening alone can be significant enough to generate shear zones in ductile rock
41 under natural conditions is debated, as well as its relative importance compared to
42 other localization mechanisms.

43 A long-lived argument against the significance of thermal softening during
44 ductile deformation in the lithosphere is that many natural shear zones with thick-
45 ness ranging from hundreds of meters to several kilometers do not indicate a
46 sharp change in temperature between the little-deformed wall rock and the highly-
47 deformed shear zone. This argument persists, despite the fact that several thermo-
48 mechanical studies have shown that even if a shear zone is caused by thermal
49 softening, there are only small temperature gradients between the shear zone and
50 the wall rock (e.g., Yuen et al. 1978; Takeuchi and Fialko 2012; Schmalholz and
51 Duretz 2015; Mako and Caddick 2018). Another argument against the importance
52 of thermal softening is that the required shear stresses or the required strain rates
53 are too large for typical lithospheric deformation conditions (e.g. Platt, 2015).

54 To test the validity of the above arguments against thermal softening and to
55 quantify thermal softening, we use a thermo-mechanical numerical model of duc-
56 tile rock deformation based on the conservation equations of continuum mechan-
57 ics and apply constitutive equations for ductile creep. We perform a scaling anal-
58 ysis with results of a one-dimensional (1D) model for which simple shearing is
59 controlled by a boundary velocity and strain localization can be triggered by a
60 temperature, hence viscosity, perturbation in the model center. We apply a temper-
61 ature perturbation because such perturbation diffuses away if shear heating is not
62 efficient. In contrast, a viscosity perturbation (i.e. perturbation of material proper-
63 ties) would remain even if shear heating is insufficient and would, hence, always

64 generate a shear zone in the 1D model, with a thickness of the initial viscosity
65 perturbation. The model configuration is based on the model of Yuen et al. (1978)
66 because for this configuration "No a priori assumption about slip-zone width or
67 shear-stress magnitude is necessary; the thermal-mechanical structure of the slip
68 zone evolves in time and all its characteristics are self consistently determined"
69 (Yuen et al., 1978). These model features are essential to study spontaneous gen-
70 eration of shear zones in homogeneous material. Yuen et al. (1978) considered
71 linear viscous flow laws only whereas we also consider power-law viscous flow
72 laws to apply our results to lithospheric dislocation creep flow laws which exhibit
73 power-law stress exponents typically between 2 and 4 (Table 1).

74 The aims of our study are to (1) quantify the temperature increase required for
75 spontaneous shear zone generation, (2) quantify the relation between the width of
76 the temperature variation across the shear zone and the width of the corresponding
77 finite strain variation, (3) quantify stresses, velocities and strain rates required
78 for shear zone generation, (4) derive an analytical formula which predicts the
79 temperature inside a shear zone without *a priori* knowledge of the thickness, stress
80 and strain rate of the shear zone, (5) compare the 1D model for bulk simple shear
81 with 2D and 3D models for bulk pure shear and (6) evaluate the importance of
82 thermal softening for ductile strain localization in the lithosphere.

83 **2. Mathematical and numerical model**

84 *2.1. Governing system of equations*

85 We assume incompressible viscous deformation in the absence of gravity and
86 inertial forces. The governing system of equations is

$$-\frac{\partial v_i}{\partial x_i} = 0 \quad (1)$$

$$-\delta_{ij} \frac{\partial P}{\partial x_i} + \frac{\partial \tau_{ij}}{\partial x_j} = 0 \quad (2)$$

$$\rho c_p \frac{\partial T}{\partial t} - \frac{\partial}{\partial x_i} \left(\lambda \frac{\partial T}{\partial x_i} \right) - \tau_{ij} \dot{\epsilon}_{ij} = 0 \quad (3)$$

$$\tau_{ij} = 2\mu_{\text{eff}} \dot{\epsilon}_{ij} \quad (4)$$

$$\mu_{\text{eff}}(\dot{\epsilon}_{\text{II}}, T) = A^{-\frac{1}{n}} \dot{\epsilon}_{\text{II}}^{\frac{1}{n}-1} \exp\left(\frac{Q}{nRT}\right) \quad (5)$$

87 where equation (1), (2) and (3) are the equations for conservation of mass, linear
 88 momentum and energy, respectively, equation (4) is the creep flow law (constitu-
 89 tive equation) and equation (5) states the effective viscosity. The indices i and j
 90 correspond to coordinate axes 1, 2 and 3 and repeated indices imply summation.
 91 In equation (3) we assume that all dissipative work is converted to heat (so-called
 92 Taylor-Quinney coefficient is 1.0) since we do not consider grain size reduction
 93 which consumes typically only a minor fraction of the dissipative work (Herwegh
 94 et al., 2014; Thielmann et al., 2015). x_i are the components of the spatial coordi-
 95 nates [m], t is the time [s], v_i are components of the velocity vector [m.s⁻¹], δ_{ij} is
 96 the Kronecker delta, τ_{ij} are components of the deviatoric stress tensor [Pa], ρ is
 97 density [kg.m⁻³], c_p is heat capacity at constant pressure [J.K⁻¹], T is tempera-
 98 ture [K], λ is thermal conductivity [W.K⁻¹.m⁻¹], μ_{eff} is effective viscosity [Pa.s],
 99 $\dot{\epsilon}_{ij}$ are components of the deviatoric strain rate tensor [s⁻¹], $\dot{\epsilon}_{\text{II}}$ is the square root
 100 of the second invariant of the strain rate tensor [s⁻¹], n is the power law exponent
 101 [], A is the pre-exponential factor [Pa ^{n} .s⁻¹], Q is activation energy [J.mol⁻¹] and
 102 R is the universal gas constant [J.mol⁻¹.K⁻¹].

Initial and boundary conditions are

$$T(\sqrt{x_i x_i} > r, t = 0) = T_0 \text{ and } T(\sqrt{x_i x_i} \leq r, t = 0) = T_0 + \Delta T_0 \quad (6)$$

$$q_i(x_i = [0 \text{ or } L_i], t) = 0 \quad (7)$$

$$v_i(x_j = 0, t) = 0 \text{ and } v_i(x_j = L_j, t) = \Delta v_i \quad (8)$$

103 where T_0 is initial temperature [K], ΔT_0 is the value of the initial temperature
104 perturbation [K], q_i are components of the heat flux vector [$\text{W} \cdot \text{m}^{-2}$], L_i is the total
105 size of the model domain [m] in the different spatial directions and Δv_i is the far-
106 field velocity difference [$\text{m} \cdot \text{s}^{-1}$] in the different spatial directions. The material
107 parameters are homogenous and the initial temperature is constant except a small
108 temperature perturbation, ΔT_0 , in a region around the model centre, $x_i = 0$, whose
109 size is specified with radius r (eq. 6, Fig.1). This thermal perturbation mimics any
110 kind of small variation of strength or thermal properties which are always present
111 in natural rocks. The model is thermally insulated (eq. 7). For simple shear
112 type deformation the model is kinematically driven by constant far-field boundary
113 velocities (eq. 8). For pure shear type deformation in 2D and 3D only velocities
114 normal to the boundaries are defined (i.e. $i = j$ for eq. 8), otherwise free slip
115 boundary conditions are used, so shear stresses are zero at the boundaries.

116 2.2. Numerical method

117 The system of non-linear equations (Eq. 1-5) is discretized on a regular Carte-
118 sian staggered grid. The problem is solved by a pseudo-transient iteration or
119 relaxation scheme (Versteeg and Malalasekera, 2007; Duretz et al., 2019). The
120 thermo-mechanical equations are recasted in the following form:

$$\begin{aligned}
\frac{dP}{d\omega} &= \frac{\partial v_i}{\partial x_i}, \\
\frac{dv_i}{d\omega} &= \frac{\partial \tau_{ij}}{\partial x_j} - \frac{\partial P}{\partial x_i}, \\
\frac{dT}{d\omega} &= \rho c_p \frac{\partial T}{\partial t} - \frac{\partial}{\partial x_i} \left(\lambda \frac{\partial T}{\partial x_i} \right) - \tau_{ij} \dot{\epsilon}_{ij}.
\end{aligned} \tag{9}$$

121 where $\frac{dP}{d\omega}$, $\frac{dv_i}{d\omega}$ and $\frac{dT}{d\omega}$ are derivatives of pressure, velocities and temperature with
122 respect to pseudo time ω . We consider here incompressible deformation in the ab-
123 sence of inertia which corresponds to the equations when the pseudo-time deriva-
124 tives have vanished. These pseudo-transient derivatives allow for an iterative solve
125 of the non-linear system of equations. At each physical time step, an explicit inte-
126 gration of the non-linear equation is carried out until the pseudo time derivatives
127 vanish and steady state is achieved. A fully implicit solution of the heat equation
128 is obtained by evaluating the heat flux and shear heating term at each pseudo-
129 transient iteration. The evaluation of temperature and strain rate dependent vis-
130 cosity is embedded within the pseudo transient iteration cycle. The pseudo tran-
131 sient algorithm is easily extendable to 2D and 3D configurations and is also well
132 suited for vectorized parallel computations (see e.g. Omlin, 2016).

133 2.3. 1D, 2D and 3D model configurations

134 The 1D model domain extends orthogonally across the shear zone and veloc-
135 ities are orthogonal to the model domain. The 1D model is driven by a velocity
136 difference at the two model boundaries which imposes a bulk simple shear de-
137 formation (Fig. 1a). To test whether results of the 1D model are applicable to
138 2D and 3D shear zones, we perform also 2D and 3D numerical simulations for
139 bulk pure shear. For the 3D model shortening occurs in one horizontal direction

140 and extension in the vertical direction while the bulk extension in the second hor-
141 izontal dimension is zero (Fig. 1c). The initial temperature perturbation has the
142 shape of a quarter circle in the 2D model (Fig. 1b) and one eighth of a sphere in
143 the 3D model (Fig. 1c). To compare the 2D and 3D results with the 1D results we
144 record the temperature and shear velocities along a profile line, with coordinates
145 x' , which is orthogonal to the 2D and 3D shear zones. These results are directly
146 comparable with the results of the corresponding 1D model (Fig. 1).

147 **3. Fundamental features of 1D shear zone evolution**

148 There are two end-member solutions of the numerical model: (1) The velocity
149 field converges to homogeneous simple shear in the entire model domain, there is
150 no strain localization and the temperature increases homogeneously in the model
151 domain due to bulk shear heating. (2) The temperature increases locally in the
152 model center, which causes strain localization and the generation of a shear zone
153 that is much thinner than the model domain. We show in the following fundamen-
154 tal features of solution (2) for representative simulations.

155 For simulations with linear viscosity the temperature increases in the shear
156 zone during a transient stage and then reaches a constant temperature (Fig. 2a), in
157 agreement with Fleitout and Froidevaux (1980). This temperature is independent
158 on the initial temperature perturbation and model width (Fig. 2a). For simula-
159 tions with power-law viscous flow laws the temperature also increases in the shear
160 zone during a transient stage and then reaches a quasi-constant temperature (Fig.
161 2b). In contrast to the linear viscous model the temperature in the shear zone
162 does not reach a strictly-constant value, but the temperature is slightly increas-
163 ing with ongoing deformation, referred to here as quasi-constant (Fig. 2b). This

164 quasi-constant temperature is also independent on the initial temperature pertur-
165 bation and the model width (Fig. 2b). For such quasi-constant temperature in the
166 shear zone center, shear heating must be locally balanced by thermal conduction
167 (Eq. 3). Fleitout and Froidevaux (1980) showed that constant boundary velocities
168 guarantee that this balance is always reached. Hence, velocity-driven shearing
169 of a dominantly viscous medium does not lead to a thermal runaway for which
170 temperatures would increase exponentially, in an unbounded way.

171 The presented model results correspond to simulations with significant shear
172 localization in the model center and show that a modest temperature rise of 100
173 °C can result in shear localization due to thermal softening (Fig. 2a and b).

174 The shear stress is spatially constant in the 1D model at each instant of time,
175 it is largest at the onset of deformation and decreases with time due to progressive
176 temperature increase due to shear heating (Fig. 2c). When the maximal temper-
177 ature reaches a quasi-constant value then also the stress reaches a quasi-constant
178 value.

179 The characteristic width of the temperature variation across the shear zone, re-
180 ferred to here as thermal thickness, is not prescribed *a priori* but controlled by the
181 thermo-mechanical process (Duretz et al., 2014, 2015). After the maximal tem-
182 perature has reached its (quasi-)constant value, the thermal thickness is increasing
183 proportional with the square root of time due to thermal conduction (Fig. 3a). In
184 the following, we distinguish between the thermal thickness and the finite strain
185 thickness that is determined by the width of the finite strain profile (Fig. 4a). The
186 thermal thickness is defined as the width of the temperature profile at this temper-
187 ature, which is half between the maximal temperature in the shear zone center and
188 the minimal ambient temperature far away from the shear zone (Fig. 3a). During

189 the transient stage of temperature increase the thermal thickness is typically de-
190 creasing (Fig. 3b). The thermal thickness evolution is essentially unaffected by
191 the initial temperature perturbation and model size, similar to the evolution of the
192 maximum temperature (Fig. 3b).

193 The temperature profile is significantly wider than the corresponding finite
194 strain (γ) profile across the shear zone (Fig. 4a), which agrees with results of
195 Takeuchi and Fialko (2012) for strike slip zones and of Schmalholz and Duretz
196 (2015) for thrust-type shear zones. γ is calculated by time integration of the shear
197 strain rates. The finite strain thickness is measured in the same way as the thermal
198 thickness, that is, the width of the γ -profile at the value of γ half between the
199 maximum value and the far-field value at the model boundary (Fig. 4a). The
200 ratio of thermal to finite strain thickness increases during the transient phase of
201 temperature increase. Once the temperature has reached its (quasi-)constant value
202 this ratio converges towards a constant value. This shows that the finite strain and
203 thermal thickness are linked, both are controlled by thermal conduction. After the
204 transient phase, the thermal thickness is nearly one order of magnitude (factor 6 to
205 8) larger than the finite strain thickness (Fig. 4b). The example presented in figure
206 4a shows that a significant decrease of γ from ca. 17, in the shear zone center, to
207 1 is associated with only a minor temperature decrease from ca. 800 °C to 760 °C
208 (i.e. only a 20% decrease).

209 **4. Predictive scaling relationships and localization criterion**

210 We performed a series of 1D numerical simulations with a geologically appli-
211 cable range for all independent model parameters: Δv , A , ρ , c_p , λ , T_0 , n and Q .
212 For each parameter we used several representative values which were evenly dis-

213 tributed within the chosen range (e.g.: $n = \{1, 2, 3, 5, 6\}$). To test the usefulness of
 214 several different sets of independent scales, we performed these simulations using
 215 the dimensional form of equations (4), (5) and (9). We run 1D simulations with all
 216 parameter combinations and recorded characteristic parameter values (e.g.: T_{\max} ,
 217 μ_{\min}) in regular intervals during shear zone evolution. We recorded data from
 218 more than 45'000 simulation stages (i.e. at specific times) from ca. 2'000 simula-
 219 tions.

220 4.1. Thermal thickness of shear zones

221 All simulations show that shear zones are widening proportional to the square
 222 root of time (Fig. 3) and that widening is controlled by heat conduction. Two fun-
 223 damental types of conductive heat transfer between shear zone and surrounding
 224 region can be distinguished: (1) If there is no significant shear heating, then the
 225 initially higher temperature in the model center is decreasing with respect to the
 226 far-field temperature during shearing and the temperature evolution in the model
 227 can be approximated with an analytical solution for Gaussian cooling of an initial
 228 Dirac delta temperature profile (Fig. 5a). The spatial and temporal evolution of
 229 temperature can then be described by the equation:

$$\Delta T(x, t) = \frac{1}{\sqrt{4\pi\kappa t}} \exp\left(-\frac{x^2}{4\kappa t}\right) \quad (10)$$

230 If the maximum temperature is in the model center, at $x = 0$, then the half
 231 width of the temperature profile is given by the value of x for which $\Delta T(x, t) =$
 232 $0.5 \Delta T_{\max}(t)$:

$$\frac{\Delta T_{\max}(t)}{2} = \frac{1}{2\sqrt{4\pi\kappa t}} = \frac{1}{\sqrt{4\pi\kappa t}} \exp\left(-\frac{x^2}{4\kappa t}\right) \rightarrow \quad (11)$$

$$0.5 = \exp\left(-\frac{x^2}{4\kappa t}\right) \rightarrow x = \sqrt{-4 \ln(0.5)\kappa t} \approx 1.67\sqrt{\kappa t} \quad (12)$$

233 The corresponding full width of the Gaussian temperature profile, W_G is then:

$$W_G \approx 3.34\sqrt{\kappa t} \iff W_G/\sqrt{\kappa t} \approx 3.34 \quad (13)$$

234 (2) If there is significant shear heating, then the temperature in the model
 235 center reaches a (quasi-)constant value after a transient period (Fig. 2a and b). The
 236 temperature evolution in model can then be described with a half space heating
 237 model in which the temperature is kept constant at one side, representing the shear
 238 zone center, and the far-field temperature is the initial temperature at the model
 239 boundary. The analytical solution for the temperature evolution for such scenario
 240 quantifies the heating of a half-space, representing the region adjacent to the shear
 241 zone and is given by an error function solution (Fig. 5a):

$$\Delta T(x, t) = \Delta T_{\max} \operatorname{erfc}\left(\frac{x}{2\sqrt{\kappa t}}\right) \quad (14)$$

242 If the maximum temperature is in the model center, at $x = 0$, then the half width of
 243 the temperature profile is given by the value of x for which $\Delta T(x, t) = 0.5 \Delta T_{\max}(t)$:

$$\frac{\Delta T_{\max}}{2} = \Delta T_{\max} \operatorname{erfc}\left(\frac{x}{2\sqrt{\kappa t}}\right) \rightarrow 0.5 = \operatorname{erfc}\left(\frac{x}{2\sqrt{\kappa t}}\right) \quad (15)$$

244 Using the approximation $\operatorname{erfc}(0.48) \approx 0.5$ yields:

$$0.48 \approx \frac{x}{2\sqrt{\kappa t}} \rightarrow x \approx 0.96\sqrt{\kappa t} \quad (16)$$

245 The corresponding full width of such temperature profile, W_E , is then:

$$W_E \approx 1.92\sqrt{\kappa t} \iff W_E/\sqrt{\kappa t} \approx 1.92 \quad (17)$$

246 If thermal evolution during shearing is dominated by conductive cooling, then
 247 the width of the temperature across the shear zone will grow according to W_G ,
 248 and according to W_E if thermal evolution is dominated by shear heating. We
 249 plotted the dimensionless widths, scaled by $\sqrt{\kappa t}$, of the numerically calculated
 250 temperature profiles versus the maximal temperature difference (i.e. maximum
 251 temperature in the shear zone center minus initial temperature, ΔT) recorded in
 252 the numerical simulations (Fig. 5b). For insignificant shear heating, $\Delta T < \text{ca. } 20$
 253 $^\circ\text{C}$, the temperature profile is widening according to W_G (Fig. 5b). For significant
 254 shear heating, $\Delta T > \text{ca. } 100$ $^\circ\text{C}$, the temperature profile is widening according to
 255 W_E (Fig. 5b). Between 20 and 100 $^\circ\text{C}$ for ΔT there is a transition zone where
 256 the thicknesses are in between W_E and W_G . The boundary between the two heat
 257 transfer domains occurs at $\Delta T \approx 40$ $^\circ\text{C}$. The results, hence, indicate that a temper-
 258 ature increase of at least 40 $^\circ\text{C}$ in the shear zone is required so that shear heating
 259 dominates the heat transfer across the shear zone.

260 4.2. *Maximum temperature of shear zones*

261 After a transient phase the temperature in the shear zone is (quasi-)constant.
 262 For such quasi steady state, heat production and conduction are essentially bal-
 263 anced in the shear zone, that is:

$$0 \approx \rho c_p \left. \frac{\partial T}{\partial t} \right|_{x=0} = \lambda \left. \frac{\partial^2 T}{\partial x^2} \right|_{x=0} + \mu \left. \left(\frac{\partial v}{\partial x} \right)^2 \right|_{x=0}. \quad (18)$$

264 For this quasi steady state, we want to determine a scaling relationship between
 265 the term representing diffusion (with λ in Eqn. 18) and the term representing shear
 266 heating (with μ). Such relationship can be of the form:

$$\lambda T_c \approx a \mu_c v_c^2 \quad (19)$$

267 where the subscripts c indicate a characteristic value of the corresponding param-
 268 eter, and a is a proportionality constant. The characteristic length scale has been
 269 dropped because it has the same power in both terms for diffusion and heat pro-
 270 duction (right side of Eqn. 18). Because the quasi steady state occurs only in the
 271 shear zone center, it is reasonable to chose characteristic values that are represen-
 272 tative for this location. There are several formally correct and reasonable choices
 273 for the characteristic values, but after testing the scaling relationship (19) with
 274 the numerical results, we found that $T_c = RT_{\max}^2/Q$, $v_c = \Delta v$ and $\mu_c = \mu_{\min}$
 275 provides the best fit. T_{\max} and μ_{\min} are always the maximal temperature and min-
 276 imum viscosity, respectively, in the shear zone center. Based on equation (19) and
 277 these characteristic values, T_{\max} can be predicted with:

$$T_{\max} \approx \frac{\Delta v}{e} \sqrt{\frac{\mu_{\min} Q}{\lambda R}} \quad (20)$$

278 where $e \approx 2.72$ is the Euler number, and e^{-1} is the proportionality constant a (Fig.
 279 6a). All parameters in this formula correspond to a specific time during shear
 280 zone evolution. Equation 20 is useful in applications where a shear zone viscosity
 281 (μ_{\min} as a function of T_{\max} and $\dot{\epsilon}_{\text{IImax}}$ or τ_{II}) can be constrained, for example, for
 282 rock deformation experiments. For most natural shear zones viscosities cannot
 283 be easily constrained. This is because, for example, for power-law viscous flow
 284 knowledge of the strain rate is required to determine the effective viscosity. We
 285 approximate the strain rate by the ratio of $\Delta v/\sqrt{\kappa t}$ assuming that $\sqrt{\kappa t}$ provides a
 286 representative value for the shear zone thickness. Using then the dataset from all
 287 the 1D simulations we determine a formula to fit the shear zone viscosity:

$$\mu_{\min} \approx 1.28 \frac{e^2 \lambda Q}{\Delta v^2 n^2 R} \left[\ln \left(\frac{\Delta v^2 n R}{\lambda Q} A^{-\frac{1}{n}} \left\{ \frac{\Delta v}{\sqrt{\kappa t}} \right\}^{\frac{1}{n}-1} \right) + 1.1 \right]^{-2}. \quad (21)$$

288 For $n = 1$ the term with the approximate strain rate disappears. If we substitute
 289 the approximation of the shear zone viscosity in equation (20) we get:

$$T_{\max} \approx -1.13 \frac{Q}{nR} \left[\ln \left(\frac{\Delta v^2 n R}{\lambda Q} A^{-\frac{1}{n}} \left\{ \frac{\Delta v}{\sqrt{\kappa t}} \right\}^{\frac{1}{n}-1} \right) + 1.1 \right]^{-1} \quad (22)$$

290 Crosschecking with the numerical results provides the minus sign for taking the
 291 square root of μ_{\min} in Eqn. 20. Equation 22 predicts the maximum temperature
 292 in all numerically simulated shear zones with a maximal error of < 50 °C and
 293 with a root mean square error of only 20 °C (Fig. 6b). The prediction of T_{\max}
 294 using equation (22) does not require any *a priori* knowledge of the shear zone
 295 thickness, the stress, the strain rate and the effective viscosity in the shear zone.
 296 The great advantage of equation (22) is, hence, that T_{\max} inside a shear zone can be
 297 estimated exclusively with flow law parameters (n , A and Q), thermal parameters
 298 (λ and c_p), the density (ρ), the applied boundary velocity difference (Δv) and the
 299 duration (t) of shearing.

300 4.3. Localization criteria

301 A possible criterion for shear localization is that shear heating must dominate
 302 the heat transfer between shear zone and the surroundings. Based on the results
 303 discussed in the previous section we suggest $T_{\max} - T_0 > 50$ °C as localization
 304 criterion. An alternative criterion can be derived by separating the variables and
 305 the constant e in equation (20) and squaring both sides, which yields:

$$\frac{\Delta v^2 \mu_{\min} Q}{\lambda R T_{\max}^2} \approx e^2 \quad (23)$$

306 If the maximum temperature is replaced by the smaller initial temperature, T_0 , and
 307 the minimum viscosity by the larger initial viscosity, μ_0 , then a modified criterion

308 for shear localization is:

$$Br_1 = \frac{\Delta v^2 \mu_0 Q}{\lambda R T_0^2} > e^2 \quad (24)$$

309 The dimensionless number on the left hand side is a particular version of the
310 Brinkman number (Br_1). Several authors suggested different versions of the
311 Brinkman number as criterion of shear localization, based on scaling analyses
312 (e.g. Brinkman 1951; Gruntfest 1963; Yuen et al. 1978; Brun and Cobbold 1980).
313 Another typical version of the Brinkman number (Br_2) is Br_1 divided by the Ar-
314 rhenius exponent (Q/RT_0). The corresponding localization criterion is then:

$$Br_2 = \frac{\Delta v^2 \mu_0}{\lambda T_0} > 1 \quad (25)$$

315 We plotted the values of both Br_1 and Br_2 versus the viscosity decrease in the
316 shear zone center (μ_{\min}/μ_0) for all simulations. Both numbers are proportional to
317 the viscosity decrease (Fig. 6c), hence they are useful criteria for strain localiza-
318 tion. We prefer using the criterion $T_{\max} - T_0 > 50$ °C due to its simplicity, or
319 the criterion based on Br_1 because it has been directly derived from the analytical
320 formula (eq. 20).

321 **5. Comparison of 1D, 2D and 3D shear zones**

322 Equations 20 and 22 for predicting the temperature in the shear zone are based
323 on a 1D model, which is driven by far-field simple shear. We apply this prediction
324 to shear zones that develop in 2D and 3D models, which are driven by far-field
325 pure shear, in order to test the general applicability of the temperature prediction
326 (Fig. 7). The rate of temperature increase in the shear zone is the largest for the
327 1D model and the smallest for the 3D model. This is because in the 1D model the
328 initial thermal perturbation is at the position of the future shear zone whereas in

329 the 2D (Fig. 7d to f) and 3D (Fig. 7a to c) models the initial thermal perturbation
 330 is present only in a fraction of the future shear zones. Also, the background tem-
 331 perature increase due to bulk shear heating of the model domain is the largest in
 332 the 3D and the smallest in the 1D model (Fig. 7g to i). Nevertheless, equation 22
 333 (associated with the 1D results) accurately predicts the temperature inside the 2D
 334 and 3D shear zones after the transient stage of temperature increase. The results
 335 also confirm that the initial temperature perturbation applied in the 1D model has
 336 no impact on the maximum temperature in the shear zone because the temperature
 337 of the 2D and 3D shear zones are unaffected by the initial thermal perturbation. A
 338 comparison of profiles of the velocities parallel to the 1D, 2D and 3D shear zones
 339 shows that the thickness of the shear zones are essentially identical. Therefore,
 340 1D, 2D and 3D shear zones caused by thermal softening under both far-field pure
 341 and simple shear exhibit the same thermo-mechanical characteristics.

342 **6. Application to dislocation creep flow laws**

343 We apply equation 22 to predict the maximum temperature in shear zones us-
 344 ing typical flow laws for rock-forming minerals relevant to the lithosphere. Equa-
 345 tion (22) depends on the duration of deformation. The typical, observed time scale
 346 of deformation varies as a function of shear velocity. To make the results for dif-
 347 ferent velocities comparable we assume a characteristic shear strain of 20, which
 348 is the ratio of displacement and shear zone thickness (W_γ). As a first order esti-
 349 mate we use one tenth (Fig 4b) of the characteristic thermal width $W_T = 2\sqrt{\kappa t}$
 350 (Fig. 5b) as a shear zone width. With these relationships we can determine a
 351 representative characteristic time of the deformation to reach a shear strain of 20:

$$20 = \gamma_c = \frac{t_c \Delta v}{0.2\sqrt{\kappa t_c}} \rightarrow t_c = \left(0.2 \frac{\gamma_c \sqrt{\kappa}}{\Delta v}\right)^2 \quad (26)$$

352 which yields $t_c \approx 5$ Ma for a velocity of ≈ 1 cm.yr⁻¹.

353 For typical plate tectonic velocities in the order of few centimeters per year,
354 the flow laws for wet and dry olivine, and dry plagioclase are associated with max-
355 imum temperatures between 500 and 700 °C (Fig. 8). Such temperatures correlate
356 well with typical temperatures of highly sheared basement nappes outcropping in
357 orogens such as the Alps. Typical metamorphic peak temperature ranges between
358 500 and 650 °C (Keller et al., 2005; Manzotti et al., 2018) and reach up to 800
359 °C in the Lepontine dome (Nagel, 2008). Takeuchi and Fialko (2012) provided a
360 thorough study of the temperature anomalies around the San Andreas strike-slip
361 fault. They used heat flow and surface deformation measurements to constrain
362 their models. They conclude that a temperature increase of 160 to 375 °C, depen-
363 dent on rheology, is expected at 20 km depth for a 4 cm.yr⁻¹ long term average
364 velocity difference. These values are in a good agreement with our prediction for
365 dry anorthite and olivine and wet olivine flow laws. Flow laws for wet quartzite
366 and Westerly granite provide maximal temperatures < 300 °C in the same velocity
367 range (Fig. 8).

368 A recent study of Chu et al. (2017) provides well constrained information
369 about the duration of deformation and maximal temperature of eclogite shear
370 zones of the Taconic orogenic belt (New England). The eclogite bodies are hosted
371 in feldspar rich felsic paragneiss. The authors conclude that the P - T history of
372 the shear zones can be best explained by shear heating. Using the known dis-
373 placement, related to the known deformation time, the shear velocities can be
374 constrained to be between 25 - 70 cm.yr⁻¹. For the inferred velocity range the
375 applicable flow law for dry anorthite yields a good fit (Fig. 8).

376 Rocks that are commonly considered to result from significant shear heating

377 are pseudotachylites. They are often associated to earthquakes, having typically
378 slip velocities on the order of a m.s^{-1} (Bizzarri, 2012). Such fast deformation
379 processes are commonly considered to be dominated by frictional deformation
380 and, hence, frictional heating. However, recent progress in understanding of
381 the physics of friction suggests viscous creep on grain contacts and asperities
382 as the mechanism for velocity weakening of the friction coefficient, reported at
383 high shear-velocity ($\approx 1 \text{ m.s}^{-1}$) rock deformation experiments for various rock
384 types (Aharonov and Scholz, 2018). Moreover, a recent experimental study of
385 high shear-velocity ($\approx 1 \text{ m.s}^{-1}$) deformation of calcite reports that such fast
386 shear deformation is characterized by an initial frictional deformation followed
387 by (quasi) steady-state viscous creep (Pozzi et al., 2018). In these experiments
388 most of the strain is generated by (quasi) steady-state viscous creep. Since the
389 (quasi) steady-state temperature developing in our models is path independent
390 (Fig. 2), we can apply our viscous model result to estimate the temperatures in
391 such small-scale and high-velocity shear zones regardless of which deformation
392 mechanism dominates initially. To test the model-based temperature estimations
393 we consider natural pseudotachylites from Corsica (Andersen et al., 2008). The
394 reported peak metamorphic temperature is at least $1750 \text{ }^\circ\text{C}$. There are no reported
395 constraints on shear velocities and, therefore, we apply peak slip velocities of 4
396 m.s^{-1} (that is typical for seismic events with a displacement around 1 m), as an
397 upper limit (Bizzarri, 2012). To estimate a lower bound, we use the width of the
398 main pseudotachylite vein ($W = 1.23 \text{ cm}$), the displacement ($d = 1 \text{ m}$, yield-
399 ing $\gamma_c = d/W \approx 80$) along it and the scaling relationship between characteristic
400 width of shear zones and the duration of deformation (eq. 16). Reordering equa-
401 tion (16) yields $t = W^2/(1.92^2 \kappa) \approx 41 \text{ s}$ (assuming $\kappa \approx 10^{-6} \text{ m}^2.\text{s}^{-1}$). Using

402 this estimate of duration we can estimate the slip velocity $v = d/t \approx 0.02$ [m.s⁻¹].
403 As such estimates have typically an order of magnitude uncertainty we take a five
404 times lower value as a lower velocity bound (i.e. 4 mm.s⁻¹). Within this wide ve-
405 locity range, the predicted temperatures for most flow laws agree with the reported
406 peak temperature (Fig. 8). Clearly, there are many uncertainties and simplifica-
407 tions related to this temperature estimate, but this estimate nevertheless indicates
408 that peak temperatures reported for the considered pseudotachylites potentially
409 could have been generated in viscous shear zones for typical slip velocities, in the
410 order of 1 m.s⁻¹.

411 Whether shear heating causes shear localization depends on the initial temper-
412 ature of the rock because localization will not occur if the ambient rock temper-
413 ature at the onset of shearing is larger than the predicted maximum temperature.
414 We consider typical lithospheric geotherms and temperatures for the upper crust
415 between 200 and 400 °C, for the lower crust between 400 and 600 °C and for the
416 mantle lithosphere > 600 °C. For typical plate tectonic velocities, we calculate
417 the predicted maximum temperature for different initial temperatures represent-
418 ing the ambient temperature at the onset of deformation (Fig. 9a). The tempera-
419 ture difference, ΔT , between predicted maximal temperature and initial, ambient,
420 temperature indicates the intensity of shear heating and, hence, shear localiza-
421 tion by thermal softening. Shear heating is significant for $\Delta T > 50$ °C since for
422 such values of ΔT the heat transfer between shear zone and wall rock is domi-
423 nated by shear heating (Fig. 5b). For plate tectonic velocities of a few cm.yr⁻¹,
424 shear heating is always important in all three lithospheric units (Fig. 9a). As ex-
425 pected, for the same velocity shear heating is always more intense in the upper
426 and colder regions of the lithospheric units. For example, for a velocity difference

427 of 3 cm.yr^{-1} the expected temperature increase in a lower crust made of ca. 400
428 $^{\circ}\text{C}$ hot anorthite is between 100 and 150 $^{\circ}\text{C}$ (Fig. 9a).

429 Shear heating is even more important if we consider a thinned thermally re-
430 laxed continental lithosphere, for example, at a passive continental margin. This
431 is because the temperatures at the top of the lower crust and mantle lithosphere
432 are colder than for a normal continental lithosphere (Fig. 9b).

433 We also analyze the initial stresses for configurations for which shear heating
434 and strain localization is significant (Fig. 9c and d). We consider scenarios for
435 which $\Delta T > 50 \text{ }^{\circ}\text{C}$ and for which initial shear stresses, τ_{xy} , are $< 1 \text{ GPa}$ (Fig.
436 9c and d). The initial shear stresses are the largest stresses during shear zone
437 formation since stress magnitudes decrease during shear zone formation due to
438 thermal softening (Fig. 2c). We assume a velocity difference of 3 cm.yr^{-1} and
439 vary initial bulk strain rates by varying the 1D model size, L . For flow laws of
440 wet anorthite shear heating is significant for ambient temperatures between 380
441 and 470 $^{\circ}\text{C}$ and for strain rates, $\dot{\epsilon}$, between 10^{-16} and 10^{-13} s^{-1} . For example, for
442 typical tectonic strain rates $\dot{\epsilon} = 10^{-15} \text{ s}^{-1}$ shear localization by thermal softening
443 is significant for shear stresses between 200 and 400 MPa for ambient temperature
444 between 420 and 470 $^{\circ}\text{C}$ (Fig. 9c). For dry olivine and for $\dot{\epsilon} = 10^{-15} \text{ s}^{-1}$ thermal
445 softening is significant for shear stresses between 200 and 400 MPa for ambient
446 temperature between 540 and 570 $^{\circ}\text{C}$ (Fig. 9d).

447 Our results indicate that the shortening of a tectonic plate, for example around
448 a thinned passive continental margin, can likely generate significant shear heat-
449 ing and associated spontaneous shear zone generation by thermal softening. Such
450 shear zone generation can take place in the ductile regime without reaching a
451 brittle-plastic yield stress. Ductile strain localization by thermal softening could

452 cause the generation of subduction zones, which is supported by numerical simu-
 453 lations (e.g. Thielmann and Kaus 2012).

454 7. Discussion

455 7.1. Localization criterion and Brinkman number

456 We already suggested the use of $T_{\max} - T_0 > 50^\circ\text{C}$ or $Br_1 > e^2$ as localiza-
 457 tion criterion. Different versions of the Brinkman number (e.g. Brinkman 1951;
 458 Grunfest 1963; Yuen et al. 1978; Brun and Cobbold 1980) have been proposed
 459 and are also known under different names, for example, Grunfest number (Gr).
 460 Using the relations $\Delta v = \dot{\epsilon}_0 L$ and $\tau_0 = \mu_0 \dot{\epsilon}_0$, several Brinkman numbers can be
 461 formulated:

$$Br_2 = \frac{\Delta v^2 \mu_0}{\lambda T_0} = \frac{\Delta v^2 \mu_0}{\lambda T_0} \frac{L^2}{L^2} = \frac{\dot{\epsilon}_0^2 \mu_0 L^2}{\lambda T_0} = \frac{\dot{\epsilon}_0 \tau_0 L^2}{\lambda T_0} = \frac{\tau_0^2 L^2}{\mu_0 \lambda T_0} = Gr \quad (27)$$

462 The right-most version with the square of the stress is often termed Grunfest
 463 number, Gr . All parameters with the subscript 0 are initial, bulk values before
 464 the occurrence of strain localization or shear zone formation. The parameter L
 465 is the model size and not the thickness of the shear zone. The same exercises
 466 can be repeated by dividing equation (27) with the dimensionless Arrhenius term
 467 Q/RT_0 , and it would result in several forms of Br_1 (equation 24). A particular
 468 localization criterion would be

$$\frac{Q}{RT_0} \frac{L^2 \dot{\epsilon}_0 \tau_0}{\lambda T_0} > e^2, \quad (28)$$

469 which is identical to the criterion of Karato (2008), if e^2 on the right hand side
 470 is replaced by 1. The different versions of the Brinkman number are useful for
 471 different deformation scenarios. For example, if the deformation is driven by

472 an applied shear stress, then the version with the square of the stress, i.e. Gr ,
473 is useful. If the thickness of the shear zone is *a priori* defined by the model
474 or experimental configuration, then a version including L is useful whereby L
475 then represents the pre-defined shear zone thickness. In general, for kinematically
476 driven models, we prefer versions without any length scale L , because the model
477 size does not affect the shear zone evolution (Fig. 2a and 2b).

478 Our results show the applicability of three different localization criteria. As
479 example, we use $Br_2 > 1$ (Fig. 6c). Applying a typical plate tectonic velocity
480 of 3 cm.yr^{-1} , an effective viscosity of $2 \times 10^{23} \text{ Pa.s}$, a thermal conductivity of 3
481 $\text{W.m}^{-1}\text{K}^{-1}$ and an ambient temperature of $500 \text{ }^\circ\text{C}$ (773 K) yields $Br_2 \approx 78$. Our
482 results show that for this value of Br_2 shear zone generation by thermal softening
483 can occur (Fig. 6c). Using a typical tectonic strain rate of 10^{-15} s^{-1} , and the ap-
484 plied effective viscosity of $2 \times 10^{23} \text{ Pa.s}$ generates a shear stress of 400 MPa , which
485 is a feasible flow stress for the upper and colder regions of the mantle lithosphere
486 or the lower crust. Indeed, the spontaneous generation of km-scale shear zones
487 by thermal softening was demonstrated in 2D thermo-mechanical simulations of
488 lithospheric shortening for viscoelastoplastic rheology (Jaquet et al., 2017; Jaquet
489 and Schmalholz, 2017).

490 Here, we do not consider viscoelastic effects. However, it was shown that elas-
491 ticity can significantly impact thermally-induced strain localisation (Regenauer-
492 Lieb and Yuen, 1998; Duretz et al., 2015; Jaquet et al., 2015) so that strain local-
493 ization can be even more significant than predicted by our localization criteria.

494 7.2. Shear zone thickness

495 A ductile shear zone is commonly observable in the field, or experiment, by the
496 significant variation of finite strain across the shear zone. The width of the varia-

497 tion of finite strain across the shear zone is nearly one order of magnitude smaller
498 than the corresponding width of the temperature variation (Fig. 4b). For signifi-
499 cant shear heating the finite strain thickness, W_γ , is ca. $2\sqrt{\kappa t}/7$ (Figs. 4b and 5b).
500 We assume that the observable width of a shear zone is determined by values of
501 finite strain > 1 . Based on Fig. 4a this observable thickness is approximately 2 to
502 3 times thicker than W_γ . Assuming a typical thermal diffusivity of $10^{-6} \text{ m}^2.\text{s}^{-1}$
503 yields $W_\gamma = \text{ca. } 1.5 \text{ km}$ and, hence, an observable thickness of 3 to 4.5 km for a
504 shear zone which is active for 1 Ma. For a shear zone which is active for 4 Ma
505 $W_\gamma = \text{ca. } 3 \text{ km}$ and the observable thickness is 6 to 9 km. Since W_γ only depends
506 on time and is independent on the applied shear velocity it can be applied to any
507 shear velocity and displacement. For example, a shear displacement of 100 km
508 for a shear velocity of 2.5 cm.yr^{-1} requires 4 Ma, for which the observable thick-
509 ness is 6 to 9 km. A shear zone with such thickness, velocity and displacement
510 is likely typical for major lithospheric shear zones related to subduction zones.
511 Such thickness relation only applies to depth levels in the lithosphere for which
512 thermal softening controls the strain localization. These durations of shear zone
513 activity and corresponding predicted shear zone thicknesses agree also with those
514 formed by thermal softening in 2D thermo-mechanical numerical simulations of
515 lithospheric shortening (Jaquet and Schmalholz 2017; Jaquet et al. 2017). Based
516 on the same relationship we expect sub-mm thickness for all shear zones that have
517 been active for less than a few seconds.

518 If natural shear zones would have been formed by thermal softening with mod-
519 erate temperature increase of 75 to 150 °C, then there would be no significant tem-
520 perature variation between the shear zone and its wall rock because natural shear
521 zones are observable due to the significant finite strain variation. This difference

522 between finite strain and temperature variation explains why many ductile shear
523 zones do not exhibit a significant observable temperature variation. The lack of a
524 sharp and observable temperature variation, for example expressed by variation in
525 metamorphic grade, is not a sufficient argument against the importance of shear
526 heating and thermal softening.

527 *7.3. Thermal softening and grain size reduction*

528 There is still ongoing dispute concerning the primary mechanism of ductile
529 strain localization in the lithosphere. Alternative to thermal softening, grain size
530 reduction in combination with mechanisms, such as pinning, that prohibit grain
531 growth (generally referred to as damage) is often proposed as primary strain local-
532 ization mechanism. Clearly, in nature both mechanisms act simultaneously. We
533 argue that thermal softening is a suitable mechanism for spontaneous strain local-
534 ization in essentially homogeneous material whereby only minor heterogeneities
535 can trigger strain localization. Grain size reduction can assist thermal softening
536 and grain size reduction is likely a mechanism that is important during progressive
537 shear zone evolution and can decrease the widening rate of the finite strain profile
538 due to heat conduction. For example, Thielmann et al. (2015) studied numerically
539 the formation of shear zones by thermal runaway using a combined approach of
540 thermal softening and grain size reduction. They showed that grain size reduction
541 reduces the stress required for thermal runaway and hence assists ductile shear
542 zone formation by thermal softening. Currently, different grain size evolution
543 models are applied, for example, Thielmann et al. (2015) apply the so-called pa-
544 leowattmeter model in which grain size is a function of flow stress, strain rate and
545 temperature, whereas Platt (2015) applies a piezometer in which grain size de-
546 pends on flow stress only. To reliably quantify the impact of grain size evolution

547 better constrained grain size evolution models for various rock types are needed.

548 **8. Conclusions**

549 A ductile shear zone which is generated spontaneously by thermal softening
550 during a velocity-driven bulk deformation exhibits the following fundamental fea-
551 tures: (1) After a transient period of temperature increase the temperature in the
552 shear zone remains constant for linear viscous flow and quasi-constant for power-
553 law viscous flow. (2) The shear stress in the shear zone is largest at the onset of
554 shear zone formation and subsequently decreases towards a (quasi-)constant value
555 associated with the establishment of a (quasi-)constant temperature. (3) The width
556 of temperature variation across the shear zone is 6 to 8 times wider than the varia-
557 tion of the corresponding finite strain. Therefore, the shear zone does not exhibit a
558 sharp, and hence easily observable, temperature variation between highly-strained
559 shear zone and little-strained wall rock. (4) The shear zone is continuously widen-
560 ing during shearing due to thermal conduction between shear zone and wall rock.
561 (5) Shear heating starts to dominate the heat transfer between shear zone and wall
562 rock once the temperature increase in the shear zone is $> \text{ca. } 50 \text{ }^\circ\text{C}$.

563 Different versions of the Brinkman number can predict the onset of shear zone
564 generation by thermal softening. However, the Brinkman number cannot quantify
565 the temperature increase inside the shear zone and, hence, the intensity of ther-
566 mal softening. We derived a new analytical formula that predicts the maximal
567 temperature inside the shear zone. This temperature prediction requires only in-
568 formation on the bulk deformation, such as far-field velocity, flow law and thermal
569 parameters, and, therefore, no *a priori* knowledge of the shear zone itself, such as
570 thickness, flow stress and strain rate. Temperature predictions across the scales of

571 geological velocities show first order agreement with several natural shear zones
572 including Alpine basement nappes, eclogite shear zones and pseudotachylites. We
573 show with 1D, 2D and 3D numerical simulations that this temperature prediction
574 is valid for shear zone generation under both bulk simple and pure shear.

575 Our results indicate that shear zone generation by thermal softening likely oc-
576 curs during lithosphere deformation in the continental lower crust and the mantle
577 lithosphere for typical lithospheric velocities of few cm.yr^{-1} or bulk strain rates
578 between 10^{-16} and 10^{-14} s^{-1} . For these deformation conditions, shear stresses of
579 few hundred MPa can already cause shear zone generation by thermal softening.

580 Based on our results and their application to lithospheric flow laws and de-
581 formation conditions, we argue that spontaneous shear zone generation by ther-
582 mal softening is a feasible and likely the primary mechanism for spontaneous
583 lithospheric scale shear zone generation. Thermal softening is probably a key
584 constituent of subduction initiation, for example, at a thinned passive continental
585 margin. Additional processes, such as grain size reduction, fabric development
586 or fluid-related reactions can cause additional softening during progressive shear
587 zone evolution and likely intensify the strain localization.

588 **9. Acknowledgements**

589 We thank an anonymous reviewer for constructive and helpful comments. This
590 work was supported by SNF grant No. 200020-149380 and the University of
591 Lausanne. We thank Ludovic Räss for assistance in performing the 3D numerical
592 simulations.

593 **References**

- 594 Aharonov, E., Scholz, C. H., 2018. A physics-based rock friction constitutive law:
595 Steady state friction. *Journal of Geophysical Research: Solid Earth* 123 (2),
596 1591–1614.
- 597 Andersen, T. B., Mair, K., Austrheim, H., Podladchikov, Y. Y., Vrijmoed, J. C.,
598 2008. Stress release in exhumed intermediate and deep earthquakes determined
599 from ultramafic pseudotachylyte. *Geology* 36 (12), 995–998.
- 600 Bercovici, D., Ricard, Y., 2012. Mechanisms for the generation of plate tectonics
601 by two-phase grain-damage and pinning. *Physics of the Earth and Planetary*
602 *Interiors* 202, 27–55.
- 603 Bizzarri, A., 2012. Analytical representation of the fault slip velocity from spon-
604 taneous dynamic earthquake models. *Journal of Geophysical Research: Solid*
605 *Earth* 117 (B6).
- 606 Brinkman, H., 1951. Heat effects in capillary flow i. *Applied Scientific Research*
607 2 (1), 120–124.
- 608 Brown, K. M., Fialko, Y., 2012. ‘melt welt’ mechanism of extreme weakening of
609 gabbro at seismic slip rates. *Nature* 488 (7413), 638.
- 610 Brun, J., Cobbold, P., 1980. Strain heating and thermal softening in continental
611 shear zones: a review. *Journal of Structural Geology* 2 (1-2), 149–158.
- 612 Carter, N. L., Tsenn, M. C., 1987. Flow properties of continental lithosphere.
613 *Tectonophysics* 136 (1-2), 27–63.

- 614 Chu, X., Ague, J. J., Podladchikov, Y. Y., Tian, M., 2017. Ultrafast eclogite for-
615 mation via melting-induced overpressure. *Earth and Planetary Science Letters*
616 479, 1–17.
- 617 Duretz, T., Räss, L., Podladchikov, Y., Schmalholz, S., 2019. Resolving ther-
618 momechanical coupling in two and three dimensions: spontaneous strain lo-
619 calization owing to shear heating. *Geophysical Journal International* 216 (1),
620 365–379.
- 621 Duretz, T., Schmalholz, S., Podladchikov, Y., 2015. Shear heating-induced strain
622 localization across the scales. *Philosophical Magazine* 95 (28-30), 3192–3207.
- 623 Duretz, T., Schmalholz, S., Podladchikov, Y., Yuen, D., 2014. Physics-controlled
624 thickness of shear zones caused by viscous heating: Implications for crustal
625 shear localization. *Geophysical Research Letters* 41 (14), 4904–4911.
- 626 Fialko, Y., Khazan, Y., 2005. Fusion by earthquake fault friction: Stick or slip?
627 *Journal of Geophysical Research: Solid Earth* 110 (B12).
- 628 Fleitout, L., Froidevaux, C., 1980. Thermal and mechanical evolution of shear
629 zones. *Journal of Structural Geology* 2 (1-2), 159–164.
- 630 Gerya, T., 2009. *Introduction to numerical geodynamic modelling*. Cambridge
631 University Press.
- 632 Ghazian, R. K., Buiter, S. J., 2013. A numerical investigation of continental colli-
633 sion styles. *Geophysical Journal International* 193 (3), 1133–1152.
- 634 Gruntfest, I., 1963. Thermal feedback in liquid flow; plane shear at constant stress.
635 *Transactions of the Society of Rheology* 7 (1), 195–207.

- 636 Gueydan, F., Précigout, J., Montési, L. G., 2014. Strain weakening enables conti-
637 nental plate tectonics. *Tectonophysics* 631, 189 – 196, observational and Mod-
638 elling perspectives on the Mechanical properties of the Lithosphere.
- 639 Hersey, M. D., 1936. Note on heat effects in capillary flow. *Physics* 7 (11), 403–
640 407.
- 641 Herwegh, M., Poulet, T., Karrech, A., Regenauer-Lieb, K., 2014. From transient
642 to steady state deformation and grain size: A thermodynamic approach us-
643 ing elasto-visco-plastic numerical modeling. *Journal of Geophysical Research:*
644 *Solid Earth* 119 (2), 900–918.
- 645 Hirth, G., Kohlstedt, D., 2003. Rheology of the upper mantle and the mantle
646 wedge: A view from the experimentalists. *Inside the subduction Factory*, 83–
647 105.
- 648 Hirth, G., Teyssier, C., Dunlap, J. W., 2001. An evaluation of quartzite flow laws
649 based on comparisons between experimentally and naturally deformed rocks.
650 *International Journal of Earth Sciences* 90 (1), 77–87.
- 651 Jaquet, Y., Duretz, T., Grujic, D., Masson, H., Schmalholz, S. M., 2017. Formation
652 of orogenic wedges and crustal shear zones by thermal softening, associated
653 topographic evolution and application to natural orogens. *Tectonophysics*.
- 654 Jaquet, Y., Duretz, T., Schmalholz, S. M., 2015. Dramatic effect of elasticity on
655 thermal softening and strain localization during lithospheric shortening. *Geo-*
656 *physical Journal International* 204 (2), 780–784.

- 657 Jaquet, Y., Schmalholz, S. M., 2017. Spontaneous ductile crustal shear zone for-
658 mation by thermal softening and related stress, temperature and strain rate evo-
659 lution. *Tectonophysics*.
- 660 Karato, S.-i., 2008. *Deformation of Earth Materials: An Introduction to the Rhe-*
661 *ology of Solid Earth* by Shun-ichiro Karato. Cambridge University Press.
- 662 Kaus, B. J., Podladchikov, Y. Y., 2006. Initiation of localized shear zones in vis-
663 coelastoplastic rocks. *Journal of Geophysical Research: Solid Earth* 111 (B4).
- 664 Keller, L. M., Hess, M., Fügenschuh, B., Schmid, S. M., 2005. Structural and
665 metamorphic evolution of the camughera–moncucco, antrona and monte rosa
666 units southwest of the simplon line, western alps. *Eclogae Geologicae Helvetiae*
667 98 (1), 19–49.
- 668 Leloup, P. H., Ricard, Y., Battaglia, J., Lacassin, R., 1999. Shear heating in con-
669 tinental strike-slip shear zones: model and field examples. *Geophysical Journal*
670 *International* 136 (1), 19–40.
- 671 Mako, C. A., Caddick, M. J., 2018. Quantifying magnitudes of shear heating in
672 metamorphic systems. *Tectonophysics* 744, 499–517.
- 673 Mancktelow, N. S., Pennacchioni, G., 2005. The control of precursor brittle frac-
674 ture and fluid–rock interaction on the development of single and paired ductile
675 shear zones. *Journal of Structural Geology* 27 (4), 645–661.
- 676 Manzotti, P., Bosse, V., Pitra, P., Robyr, M., Schiavi, F., Ballèvre, M., 2018. Ex-
677 humation rates in the gran paradiso massif (western alps) constrained by in situ
678 u–th–pb dating of accessory phases (monazite, allanite and xenotime). *Contri-*
679 *butions to Mineralogy and Petrology* 173 (3), 24.

- 680 Montési, L. G., 2013. Fabric development as the key for forming ductile shear
681 zones and enabling plate tectonics. *Journal of Structural Geology* 50, 254–266.
- 682 Moore, J. D., Parsons, B., 2015. Scaling of viscous shear zones with depth-
683 dependent viscosity and power-law stress–strain-rate dependence. *Geophysical*
684 *Journal International* 202 (1), 242–260.
- 685 Nagel, T. J., 2008. Tertiary subduction, collision and exhumation recorded in the
686 adula nappe, central alps. Geological Society, London, Special Publications
687 298 (1), 365–392.
- 688 Omlin, S., 2016. Development of massively parallel near peak performance
689 solvers for three-dimensional geodynamic modelling. Ph.D. thesis, University
690 of Lausanne.
- 691 Platt, J., Behr, W., 2011. Grainsize evolution in ductile shear zones: Implications
692 for strain localization and the strength of the lithosphere. *Journal of Structural*
693 *Geology* 33 (4), 537–550.
- 694 Platt, J. P., 2015. Influence of shear heating on microstructurally defined plate
695 boundary shear zones. *Journal of Structural Geology* 79, 80–89.
- 696 Pozzi, G., De Paola, N., Nielsen, S. B., Holdsworth, R. E., Bowen, L., 2018.
697 A new interpretation for the nature and significance of mirror-like surfaces in
698 experimental carbonate-hosted seismic faults. *Geology*.
- 699 Regenauer-Lieb, K., Yuen, D. A., 1998. Rapid conversion of elastic energy into
700 plastic shear heating during incipient necking of the lithosphere. *Geophysical*
701 *Research Letters* 25 (14), 2737–2740.

- 702 Regenauer-Lieb, K., Yuen, D. A., Branlund, J., 2001. The initiation of subduction:
703 criticality by addition of water? *Science* 294 (5542), 578–580.
- 704 Rybacki, E., Dresen, G., 2004. Deformation mechanism maps for feldspar rocks.
705 *Tectonophysics* 382 (3), 173–187.
- 706 Schmalholz, S., Duretz, T., 2015. Shear zone and nappe formation by thermal
707 softening, related stress and temperature evolution, and application to the alps.
708 *Journal of Metamorphic Geology* 33 (8), 887–908.
- 709 Sibson, R. H., 1975. Generation of pseudotachylyte by ancient seismic faulting.
710 *Geophysical Journal International* 43 (3), 775–794.
- 711 Takeuchi, C. S., Fialko, Y., 2012. Dynamic models of interseismic deformation
712 and stress transfer from plate motion to continental transform faults. *Journal of*
713 *Geophysical Research: Solid Earth* 117 (B5).
- 714 Thielmann, M., Kaus, B. J., 2012. Shear heating induced lithospheric-scale local-
715 ization: Does it result in subduction? *Earth and Planetary Science Letters* 359,
716 1–13.
- 717 Thielmann, M., Rozel, A., Kaus, B., Ricard, Y., 2015. Intermediate-depth earth-
718 quake generation and shear zone formation caused by grain size reduction and
719 shear heating. *Geology* 43 (9), 791–794.
- 720 Versteeg, H., Malalasekera, W., 2007. *An Introduction to Computational Fluid Dy-*
721 *namics: The Finite Volume Method (2nd Edition)*. Pearson.
- 722 White, S. t., Knipe, R., 1978. Transformation-and reaction-enhanced ductility in
723 rocks. *Journal of the Geological Society* 135 (5), 513–516.

724 Yuen, D., Fleitout, L., Schubert, G., Froidevaux, C., 1978. Shear deformation
725 zones along major transform faults and subducting slabs. *Geophysical Journal*
726 *International* 54 (1), 93–119.

Lithology	A [$\text{Pa}^{-(n+r)}\text{s}^{-1}$]	n	$f_{\text{H}_2\text{O}}$ [Pa]	r	A_{eff} [$\text{Pa}^{-n}\text{s}^{-1}$]	Q [$\text{J}\cdot\text{mol}^{-1}$]	λ [$\text{W}\cdot\text{K}^{-1}\cdot\text{m}^{-1}$]	ρ [$\text{kg}\cdot\text{m}^{-3}$]
Wet quartzite ¹	6.31×10^{-42}	4.0	3.7×10^7	1	2.91×10^{-32}	1.35×10^5	2.5	2700
Westerly granite ²	3.17×10^{-26}	3.3	-	0	1.67×10^{-24}	1.87×10^5	2.5	2700
Wet albite ³	2.51×10^{-15}	3.0	-	0	9.04×10^{-14}	3.32×10^5	2.2	2900
Wet anorthite ³	3.98×10^{-16}	3.0	-	0	1.43×10^{-14}	3.56×10^5	2.2	2900
Dry anorthite ³	5.01×10^{-6}	3.0	-	0	1.80×10^{-4}	6.56×10^5	2.2	2900
Wet olivine ⁴	5.68×10^{-27}	3.5	10^9	1.2	2.40×10^{-14}	4.80×10^5	3.0	3400
Dry olivine ⁴	1.10×10^{-16}	3.5	-	0	7.37×10^{-15}	5.30×10^5	3.0	3400

Table 1: Rheological and thermal parameters for the used lithologies. $A_{\text{eff}} = FAf_{\text{H}_2\text{O}}^r d^{-p}$ is an effective pre-exponential factor (' A ' in the main text) that incorporates grain size (d) and water fugacity ($f_{\text{H}_2\text{O}}$) dependence. In all cases we use dislocation creep therefore the grain size exponent is $p = 0$. All of these flow laws describe stress and strain rate relationship in uniaxial compression experiments. In order to convert them into strain rate dependent invariant forms we need to introduce a geometry factor, which is $F = 2^{n-1}3^{(n+1)/2}$ for all presented cases (see e.g. Gerya 2009). The rest of the parameters are: power law exponent (n), water fugacity exponent (r), activation energy (Q), thermal conductivity (λ), density (ρ) and finally heat capacity is constant for all ($c_p = 1050 \text{ J}\cdot\text{kg}^{-1}\text{K}^{-1}$). The sources of the rheological parameters are: ¹Hirth et al. 2001, ²Carter and Tsenn 1987, ³Rybacki and Dresen 2004, ⁴Hirth and Kohlstedt 2003.

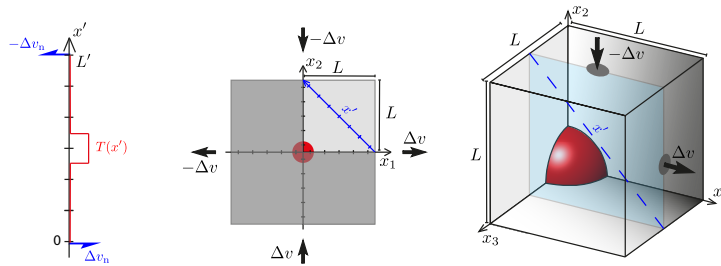


Figure 1: Model configurations for 1D simple shear, and 2D and 3D pure shear bulk deformation. In all models a thermal perturbation (red) is in the model center. Due to the symmetry of the problem we solve the 2D and 3D models only for the positive coordinate region. To compare 1D results with 2D and 3D results, the results of the 1D model are rotated so that they correspond to the direction x' in the 2D and 3D models which is orthogonal to the shear zone.

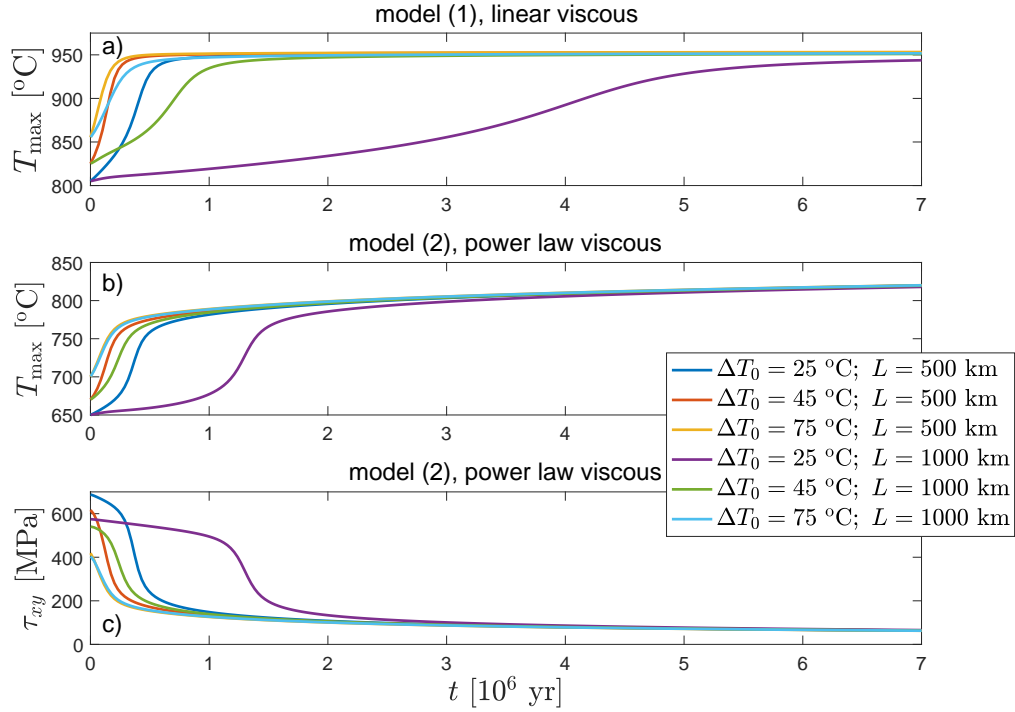


Figure 2: Representative results of 1D shear zone models. Time evolution of maximum temperature at the shear zone center for linear viscous (a) and power-law viscous (b) flow. Model (1) is based on a dry anorthite diffusion creep flow law with $A_{\text{eff}} = 0.14 \text{ Pa}\cdot\text{s}^{-1}$ ($d = 0.3 \text{ mm}$) and $Q = 467 \text{ kJ}\cdot\text{mol}^{-1}$, model (2) is based on a dry peridotite flow law (see Table 1). In both models we applied $3 \text{ cm}\cdot\text{yr}^{-1}$ velocity difference. Different lines correspond to models with different model size and initial perturbation (see legend, which applies to all three panels). After a transient stage the maximum temperature converges to a constant (a) or (quasi-)constant (b) temperature. c) Shear stress evolution for power law simulations, shown in panel b). The shear stress always decreases with progressive shear zone evolution and converges to a quasi-constant value.

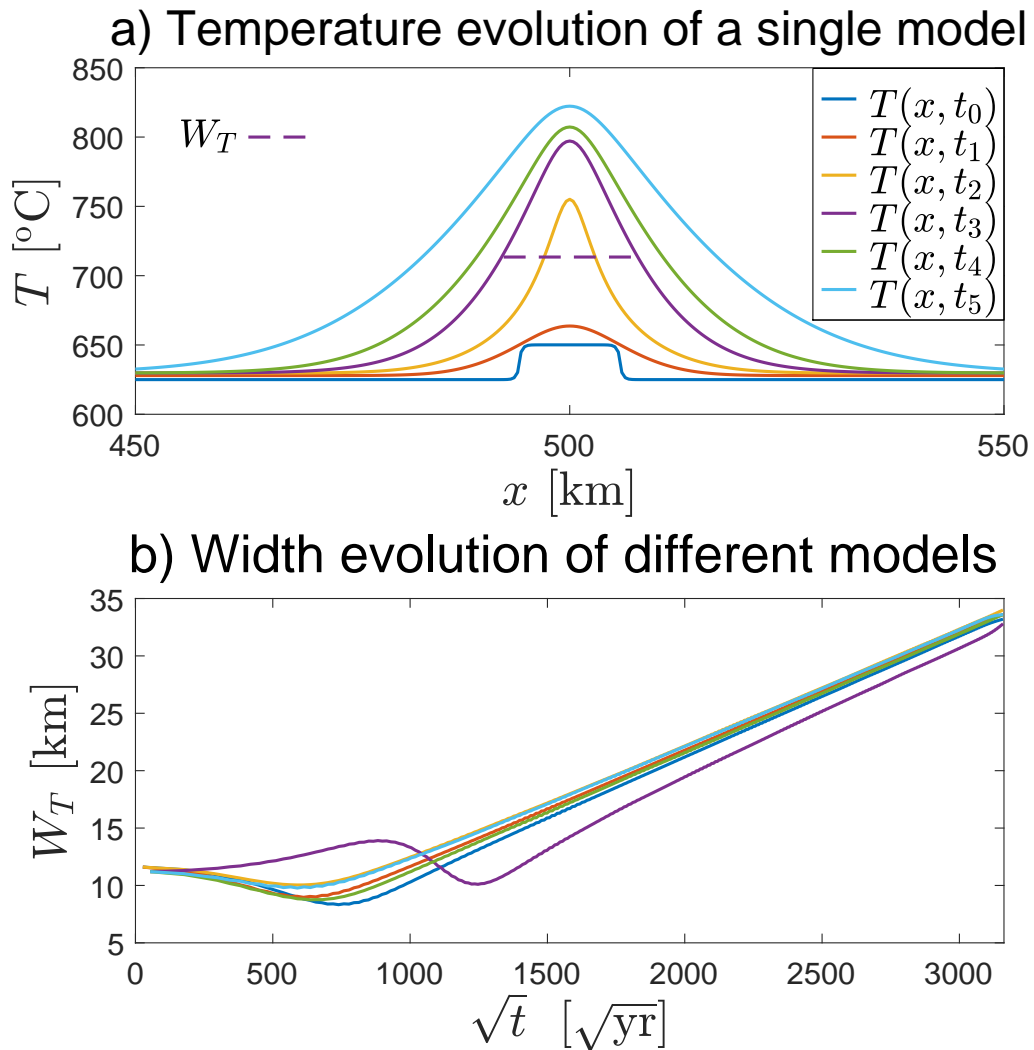


Figure 3: a) Representative time evolution of a temperature profile during shear zone formation. The model setup is equivalent with the one of the $\Delta T_0 = 25$ °C, and $L = 1000$ km from Fig. 2b and 2c. The dashed horizontal line indicates the thermal thickness which is measured at the temperature which is half between the maximum and minimum temperature of the corresponding profile. b) Evolution of thermal thickness for different representative simulations (same colors are used in Fig. 2b and 2c). Each line shows the result of a simulation with different initial temperature perturbation and model size. After a transient period, the thickness evolution for all simulations is linearly increasing with the square root of time.

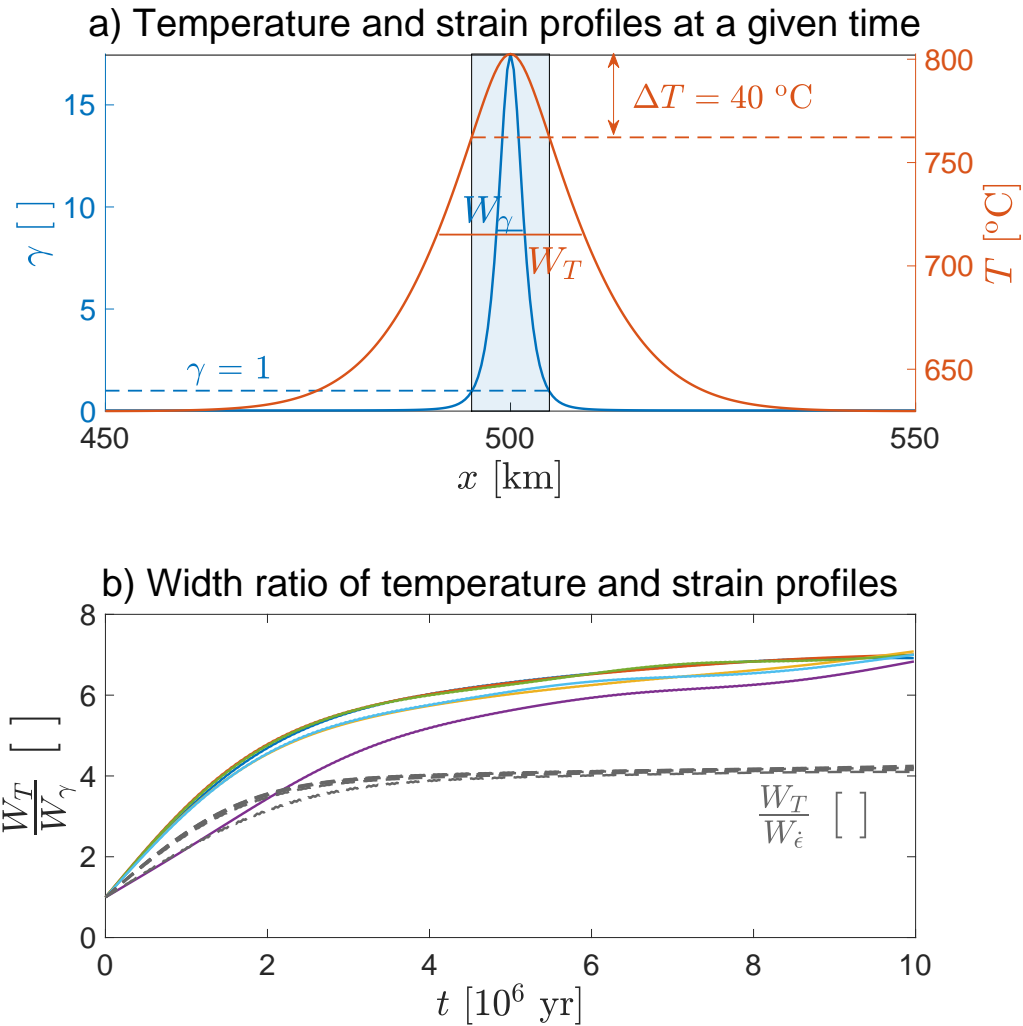


Figure 4: a) Temperature and corresponding finite strain profile for a simulation with a dry olivine flow law after 3.5 Myr. The model setup is equivalent with the one of the $\Delta T_0 = 25 \text{ }^\circ\text{C}$, and $L = 1000 \text{ km}$ from Fig. 2b and 2c. The temperature profile is significantly wider than the finite strain profile. The thickness of both profiles is measured at the vertical value which is half between the maximum and minimum value of the profile. b) Evolution of the ratio of thermal thickness to corresponding finite strain thickness with progressive time for different model configurations (colors are corresponding to Fig. 2b and 2c). After a transient stage the ratios approach values between 6 and 8 showing that the temperature variation is nearly one order of magnitude wider than the corresponding finite strain variation. For comparison, also the ratio of thermal thickness to corresponding instantaneous strain rate thickness is displayed with gray dashed lines, because this thickness ratio is constant and ca. 4 for all shown simulations.

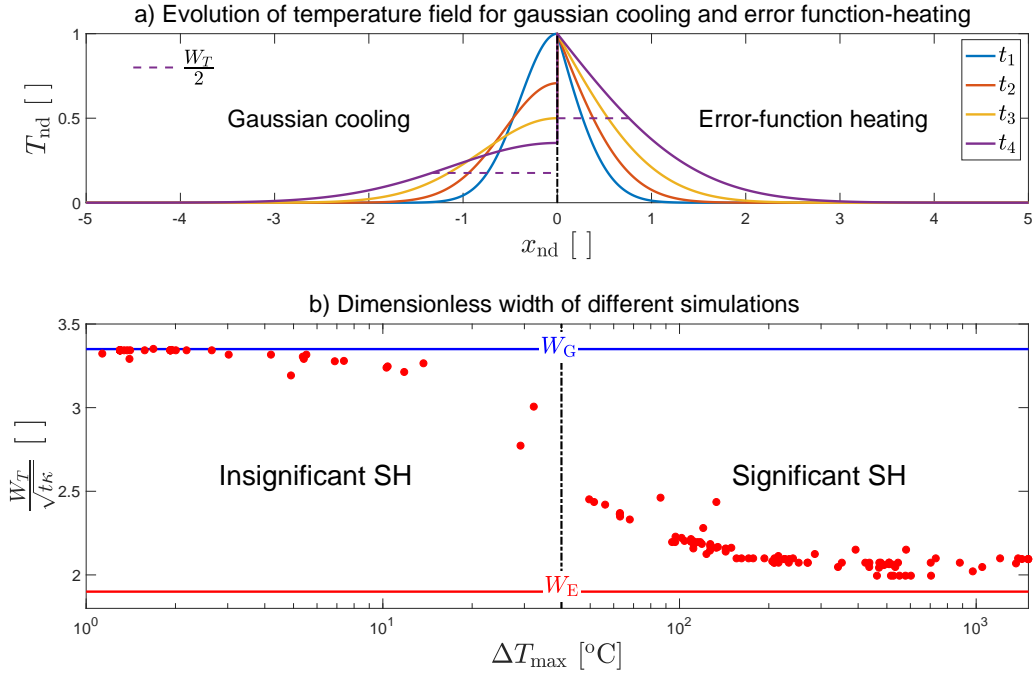


Figure 5: a) Representative temperature evolution for cooling of an initial Gaussian temperature profile, left curves, and for heating for a constant temperature in the model center, right curves. Lines for t_1 to t_4 display temperature profiles at progressive times. The dashed horizontal lines indicate the half-width of a specific temperature profile. Horizontal x-coordinates and temperatures are dimensionless and temperatures have been scaled so that the initial temperature is identical. b) Plot of the dimensionless widths of temperature profiles determined from 1D numerical simulations versus the corresponding temperature increase in the shear zone centre, ΔT_{max} . The blue and red horizontal lines indicate the theoretical dimensionless width for cooling of an initial Gaussian temperature profile (equation 13) and for heating for a constant temperature in the shear zone (equation 16), respectively. A value of $\Delta T_{max} \approx 40$ °C indicates the transition between the two types of heat transfer and for $\Delta T_{max} > 40$ °C shear heating (SH) is significant.

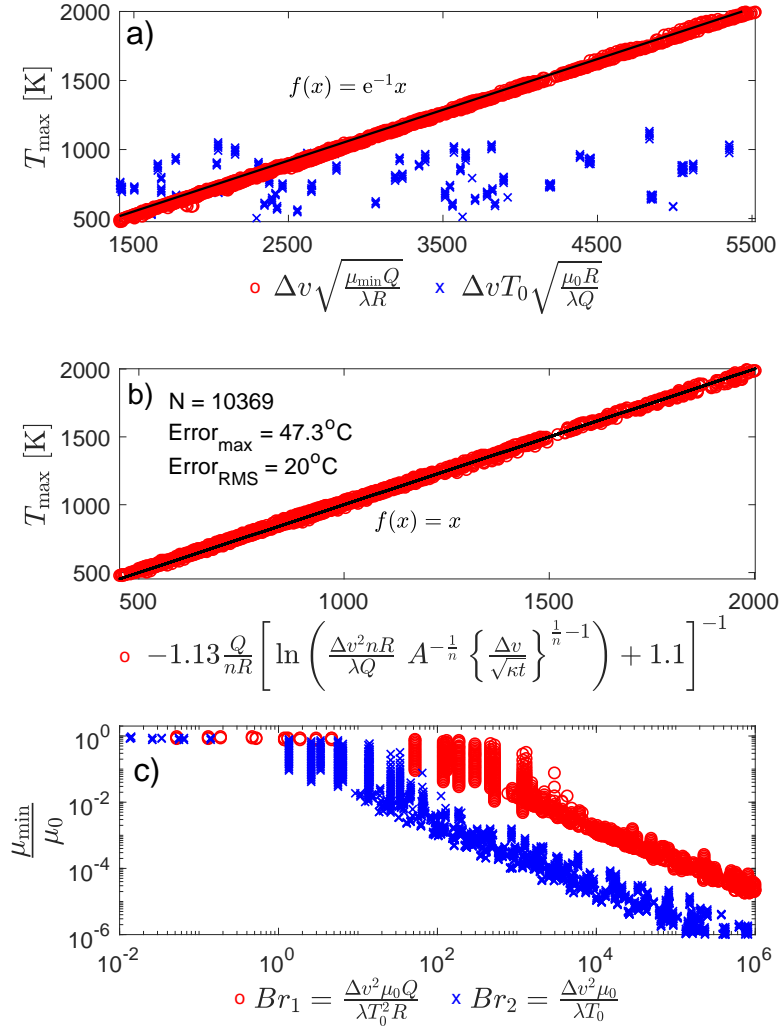


Figure 6: a) Maximum temperature versus two different characteristic temperatures for all 1D simulations. Red circles represent a choice of scales which generates a data collapse and the blue crosses are an example of a scaling that generates a data scatter. The black line indicates a fit of the data (see equation in panel) where e is the Euler number. b) Maximum temperature in the shear zone from all numerical 1D simulations (T_{\max}) versus the maximum temperature predicted with equation 22 (equation in label). c) Ratio of the minimum shear zone viscosity to the initial viscosity versus two versions of Brinkman number, Br_1 and Br_2 .

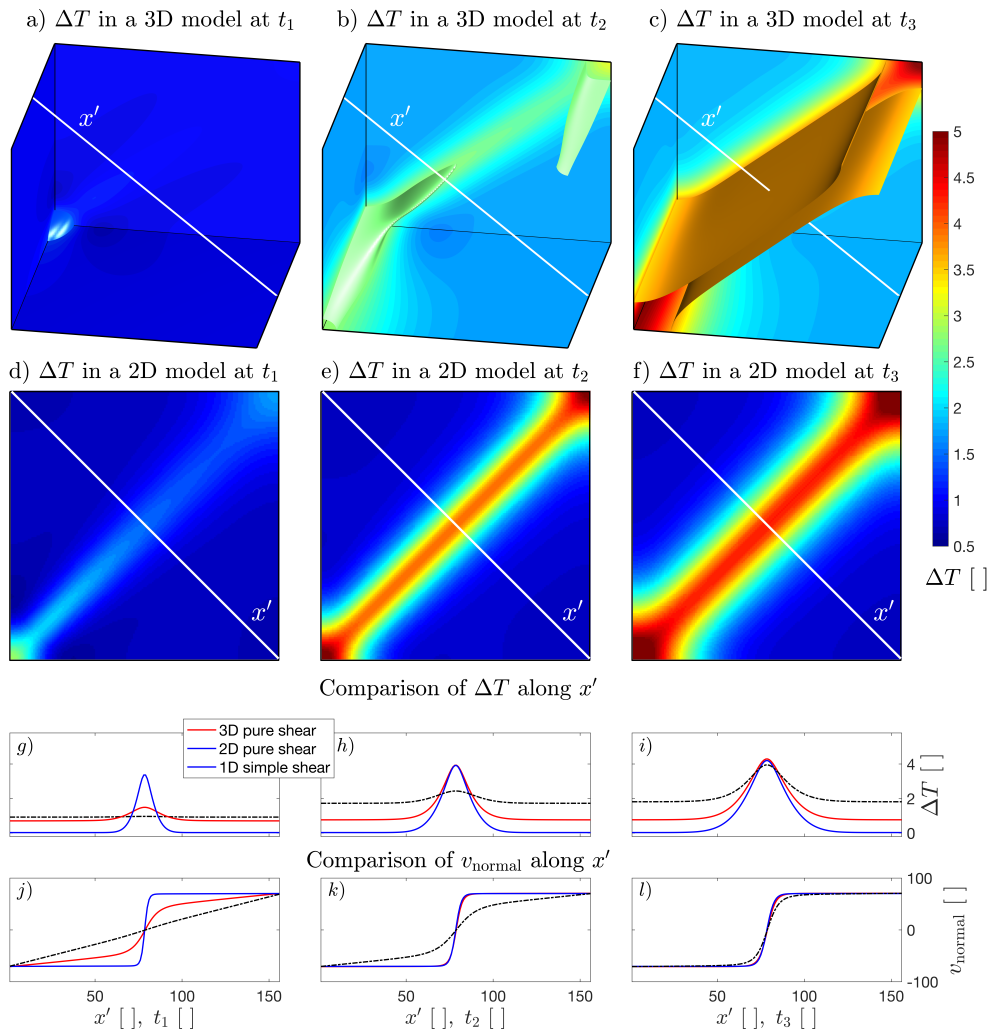


Figure 7: Comparison of temperature and velocity profiles across 1D, 2D and 3D shear zones. a) to c) shows the temperature field for three stages of 3D shear zone formation. d) to f) shows the temperature field for three stages of 2D shear zone formation. The profile lines indicated with x' in both 2D and 3D models are used for the comparison with the 1D model. g) to i) show 1D temperature profile and the 2D and 3D profiles along the x' profile for three different times. j) to l) show the 1D velocity profile and the 2D and 3D profiles along the x' -profile for three different times. The displayed velocity magnitudes are normal to the profile orientation and, hence, parallel to the shear zone orientation.

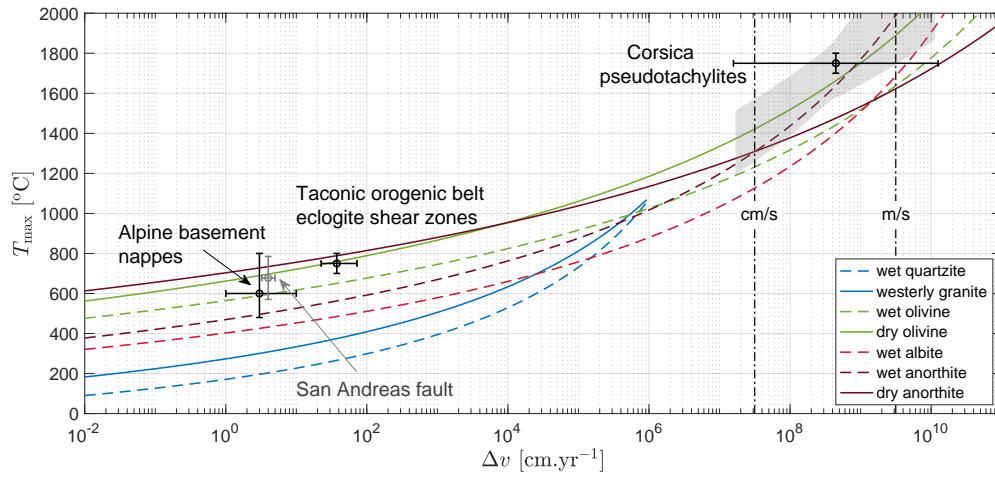


Figure 8: Predicted maximum temperature in shear zones across the scales. Four data points are shown as possible applications. Three of them are direct observations, displayed with black, while the gray is an indirect observation (see in section 6). Equation 22 is used for temperature prediction versus the applied boundary velocities, Δv , for different flow laws (see legend and Table 1). The same constant finite shear strain, $\gamma_c = 20$, is assumed for all shear zones and the corresponding duration of the deformation is calculated with equation 26. For pseudotachylites the typical values of finite strain are higher. The expected temperature range for $\gamma_c = 80$ is indicated by the light gray area. The quartzite flow laws are not displayed for high velocities because for those the argument of the logarithm is approaching $\exp(-1.1) \approx 0.3$, where the prediction starts to significantly deviate from the solution.

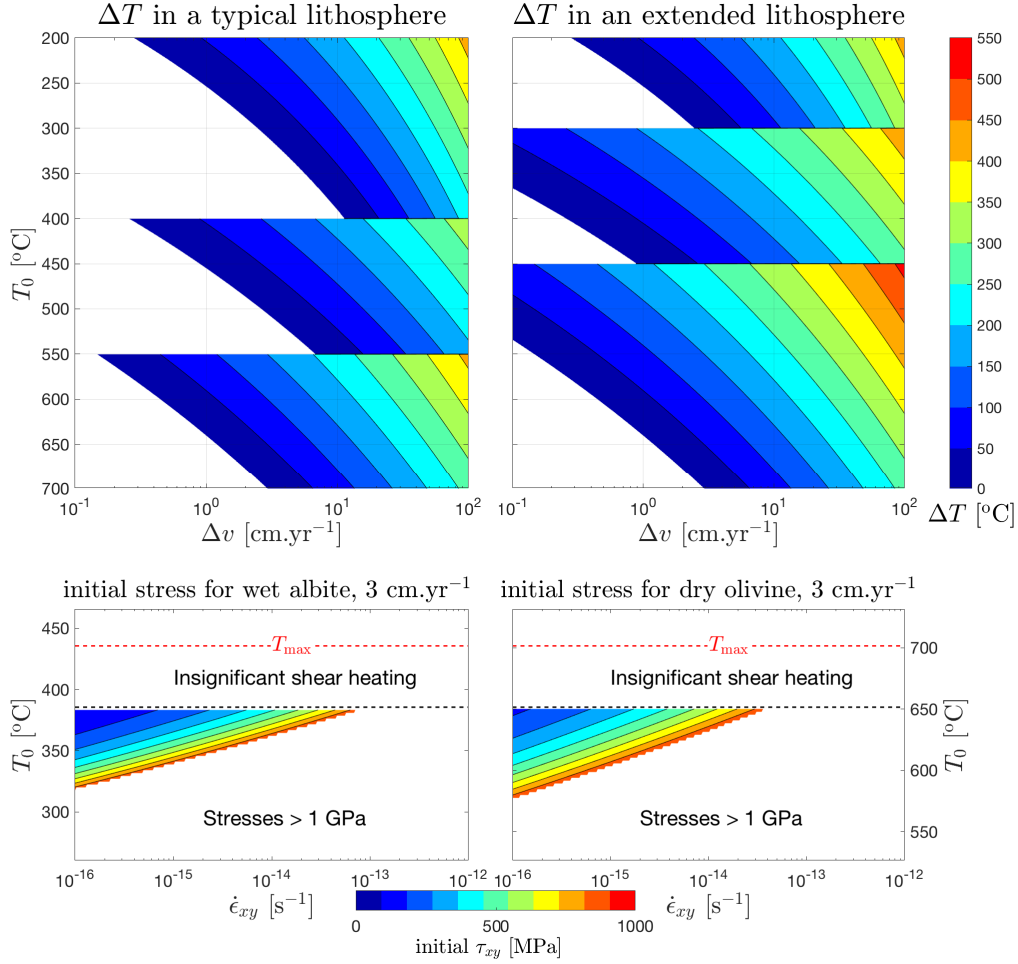


Figure 9: a) and b) show color plots of the temperature difference, ΔT , between the maximum temperature predicted with equation (22) and the initial temperature, T_0 , corresponding to the ambient temperature at a certain depth in the lithosphere. ΔT is contoured for different values of T_0 and ΔV . ΔT is calculated for a deformation time of 1 Ma. The three regions in the color plots correspond to three different flow laws, namely for Westerly granite (top region representing upper crust), wet anorthite (middle region representing lower crust) and wet olivine (lower region representing mantle lithosphere). c) and d) show color plots of the initial shear stress in 1D simulations as a function of T_0 and applied bulk strain rate, $\dot{\epsilon}_{xy}$. c) shows results for wet albite flow law and d) for dry olivine. The applied velocity difference is 3 cm.yr⁻¹ and bulk strain rates are modified by changing the 1D model size. The red dashed horizontal line indicates the maximum temperature, T_{max} , from equation (22). To have significant shear localization, T_0 must be at least 50 °C smaller than T_{max} (see Fig. 5b). Only shear stresses < 1 GPa are displayed. The colored regions in c) and d) indicate the "window" in which shear zone generation by thermal softening is feasible in the lower crust (c) and mantle lithosphere (d).